actuators

MDPI

Article

Research on Magnetic Characteristics and Fuzzy PID Control of Electromagnetic Suspension

Wei Wei *, Songjian Yu and Baozuo Li

College of Mechanical Engineering and Automation, Liaoning University of Technology, Jinzhou 121001, China
* Correspondence: jxweiwei@lnut.edu.cn

Abstract: This paper proposes an electromagnetic suspension with an electromagnetic actuator, which can improve the riding comfort and stability of the vehicle without changing the safety of traditional MacPherson suspension. First, the electromagnetic suspension structure is introduced, and the principle of the proposed actuator is described in detail. Second, a magnetic flux density model of a single PM ring (permanent magnetic ring) and a magnet assembly are built, and a theoretical analysis of the magnetic flux density is carried out for comparison. Then, the magnetic flux distribution of the magnetic field is simulated and analyzed using the finite element method (FEM), and is compared with theoretical and other experimental data. Finally, a vehicle dynamics model with 7 DOF is built, and vehicle simulations based on the fuzzy PID algorithm are carried out on a C-grade road surface and a deceleration strip. The theoretical results and simulation analyses of the FEM indicate that compared with the MacPherson suspension, the root mean square values of the acceleration of centroid acceleration for the electromagnetic suspension are increased by 59.08% and 33.34%, respectively, on a C-grade road surface and a deceleration strip, and other physical quantities have also been improved. The structure and characteristics of the proposed electromagnetic suspension that improve the riding comfort of the suspension and enhance the stability of the MacPherson suspension are feasible.

Keywords: electromagnetic suspension; quasi-parallel magnetic field; magnetic characteristics; electromagnetic actuator

Citation: Wei, W.; Yu, S.; Li, B. Research on Magnetic Characteristics and Fuzzy PID Control of Electromagnetic Suspension. *Actuators* **2023**, *12*, 203. https://doi.org/10.3390/act12050203

Academic Editor: Jun Zheng

Received: 31 March 2023
Revised: 10 May 2023
Accepted: 16 May 2023
Published: 17 May 2023

1. Introduction

The rapid growth in the number of vehicles, driven by the development of transportation and the improvement of people's quality of life, has attracted increasing attention on body vibration and tire wear. This concerns not only the safety and integrity of the goods transported by automobiles but also the riding comfort and handling stability of the vehicle [1]. As a key component of the vehicle's body, the chassis not only supports the vehicle but also accepts the thrust generated by the engine, ensuring the normal operation of the vehicle [2,3]. Suspension systems, as key components of automobile chassis, have garnered significant research interest.

Suspension systems play a key role in supporting the vehicle body and ensuring the comfort, stability, and safety of vehicles. The research and development of comprehensive suspension system performance is a key factor affecting vehicle performance, body direction and attitude control, handling stability, and the driving and riding experience. McPherson-independent suspension, widely used in the front suspension of modern cars, has several shortcomings, including small brake resistance, weak suspension stiffness, poor stability, and a noticeable turning roll. Therefore, designing a high-performance automobile suspension system can fundamentally improve the performance of an automobile [4,5]. Suspension systems are developing towards the direction of lighter weight, smaller volume, faster responses, more stable running state, and greater safety and reliability. With the development of cities and increasing road pressure, vehicles, particularly their suspension

systems, are more susceptible to problems [6]. The performance of a suspension system mainly depends on the response ability of its actuator or the motor-to-road conditions. Therefore, it is of great significance to research and discuss automobile suspension systems and their related components.

Compared with passive suspension systems, semi-active suspension systems can change the damping of shock absorbers by controlling the input of a single variable so as to adapt to different road conditions [7–9]. At present, there are two types of adjustable shock absorbers in semi-active suspension systems, which differ in terms of the amount of control they exert. One adjusts the damping size of the damper solenoid valve by adjusting the effective area of the throttle, but this method cannot avoid suspension system noise and stability and reliability problems. The other adjusts the spring rigidity of the whole shock absorber by changing the spring stiffness of the variable spring, but this may produce bumps during the driving process.

Because there are no components with controllable forces installed in the system, a semi-active suspension system cannot control the stiffness of the spring. Therefore, research on semi-active suspension is greatly limited, and the improvement of vehicle performance when using this suspension type is also greatly limited [10].

In recent years, researchers have designed various active suspension systems, including those with rack and pinion rotating motors [11–14], ball screw mechanisms [15–18], hydraulic actuating quarter-car active suspension systems [19], and electromagnetic suspension [20–22], among others. With the development of electromagnetic control technology and PM material, electromagnetic suspension as a new type of suspension structure has become of interest for researchers, such as traditional hydraulic dampers with a linear motor [23], mechanisms with a ball screw mechanism and two one-way clutches [24], coreless linear tube actuators with a special topology [25,26], electromagnetic and hydraulic suspensions [27], and rotating semi-active electromagnetic variable stiffness devices [28], and so on. They use these mechanisms instead of the dampers or springs of traditional suspensions, or even both can be used. However, safety was not considered in the event of suspension failure or power failure.

Suspension using a motor, magnetorheological fluid damper [29,30], and suspension using an electromagnetic actuator are examples of active electromagnetic suspension. Compared with the first two types of active suspension, electromagnetic actuator suspension is simpler and more efficient in terms of its structure, performance, magnetic force, processing, and so on. An electromagnetic actuator can greatly improve the reaction speed of a suspension system, and thus, it has become the research focus of more and more scholars [31,32]. In addition, electromagnetic actuators also have the advantages of simple system configuration, fast response speed, and energy recycling, and as a result, they are more and more widely used.

Integrating control methods into active suspension systems can significantly enhance their performance. In [33], the semi-active suspension of automotive magnetorheological fluids was controlled by a fuzzy control algorithm, and the overall performance of the suspension was improved. In [34], a semi-active 1/4 suspension with three degrees of freedom utilizing a magneto-rheological shock absorber was controlled by a hybrid fuzzy and fuzzy PID controller. In [35], a fuzzy PID controller was applied in a half vehicle active suspension system to enhance the vibration levels of the vehicle chassis and passenger seat. Therefore, the fuzzy PID control algorithm combines the advantages of fuzzy control and PID control, which makes it suitable for research on controlling electromagnetic suspension.

This paper aims to make up for the ride comfort and stability of the vehicle without changing the safety of the McPherson suspension. In this paper, we propose an electromagnetic suspension structure that can improve the stability and ride comfort performance of vehicles and make up for the defects of the McPherson suspension. Firstly, the structure of the proposed suspension is introduced, and its principle is described in detail. Secondly, the magnetic flux density model of a single PM ring and a magnet component is established, and the theoretical analysis of the magnetic flux density is carried out. Then, the magnetic flux distribution of the magnetic field is analyzed via the two-dimensional finite element method, and the magnetic flux density is simulated via finite element analysis. Finally, a vehicle dynamics model with seven degrees of freedom is established, and a vehicle simulation on C-grade roads and a deceleration strip is carried out based on the fuzzy PID algorithm. After improving the MacPherson suspension system, active control, four-wheel ride comfort, and stability issues were studied with C-grade roads and a deceleration strip.

2. Structure and Principle

The proposed structure of the electromagnetic actuator uses a 1/4 MacPherson-type independent suspension system, as shown in Figure 1a. The electromagnetic actuator is inserted into the gap between the hydraulic damper and the spring, the coil assembly of the electromagnetic actuator is connected with the upper cover, and the magnet assembly of the electromagnetic actuator is connected with the cylinder tube of the hydraulic damper, as shown in Figure 1b. The spring, electromagnetic actuator, and hydraulic damper are connected in parallel. The magnet assembly adopts a double-layer PM magnet ring form, and the coil assembly moves in the air gap of the magnet assembly. Compared to the magnet assembly, the coil weighs less; the coils are connected to the upper cover of the shock absorber, which facilitates connection to the vehicle's internal circuit. Consequently, the electromagnetic suspension can be controlled by inputting a current to resolve the disadvantages of the MacPherson-type independent suspension. In this application, it is necessary to maintain a safe distance between the electromagnetic actuator and the spring. When the spring compresses to its lowest point, the distance between the upper cover and lower cover is longer than the axial distance of the electromagnetic actuator, which means that it can avoid the strike of the upper cover and the lower cover at the compression limit. A characteristic of this electromagnetic suspension is that it does not change the structure of the MacPherson suspension. It not only ensures the safety of the MacPherson suspension, but it also improves the stability of the MacPherson suspension.

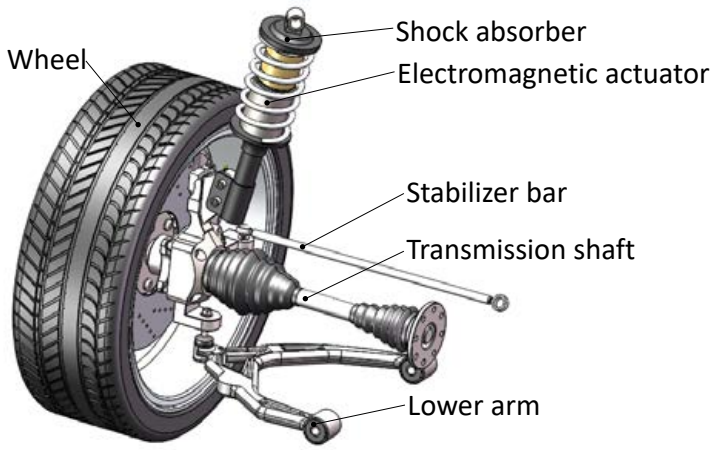

(**a**)

Figure 1. *Cont.*

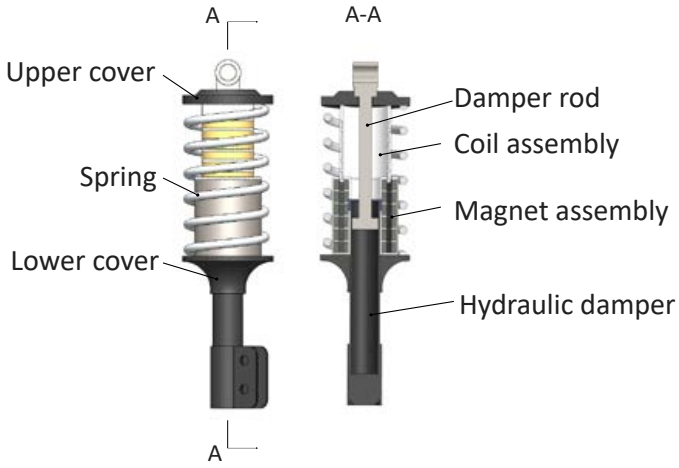

Figure 1. Structure of the electromagnetic suspension system. (**a**) 1/4 MacPherson-type independent suspension. (**b**) Electromagnetic shock absorber.

The structure of the proposed electromagnetic actuator is shown in Figure 2. The coil assembly involves a group of coils moving along the axis of the actuator. The magnet assembly consists of the outer wall, six small PM rings, and six large PM rings for radial magnetization, heat-dissipated rings, and a fixed plug. Each PM ring is composed of eight identical pieces, and their material is Nd–Fe–B, and the PM rings are magnetized inside as the S pole and the outside as the N pole. The outer wall and the fixed plug are used to fix the PM rings. The heat-dissipated ring is used for dissipating heat between two PM rings to avoid the phenomenon of heat accumulation. The fixed plug plays a role in fixing the PM rings and heat-dissipated rings. Large PM rings and small PM rings are placed side by side; the magnet assembly can generate a quasi-parallel magnetic field.

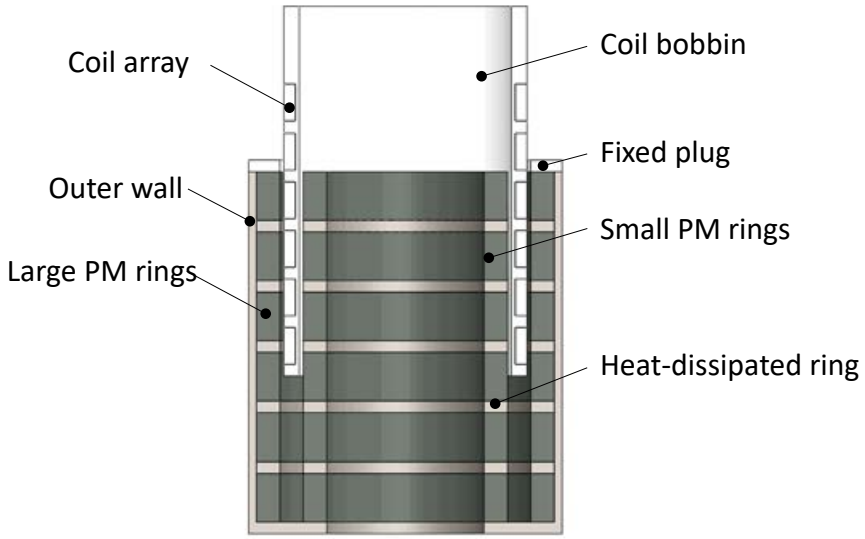

Figure 2. Structure of the magnet assembly.

2.1. Design of the Electromagnetic Actuator

For electromagnetic actuators, it is necessary to achieve a compact size and a large magnetic force. The influence of the height and radial length of large/small PM rings and the height of coils on the magnetic force of the proposed actuator was analyzed using orthogonal experimental methods. As shown in Table 1, height and radial length of large/small PM rings and the height of coils were determined as three factors for the orthogonal experimental method, with each factor having three levels. The simulation parameters are that the coercivity of the PM ring is 868 KA/m and the residual magnetic flux density of the PM ring is 1.38–1.44 T. The L_9 ($3^2 \times 3^2$) size optimization simulations of the actuator by the orthogonal experiment method are shown in Table 2.

Table 1. Factors and levels in the orthogonal experiment method.

Level	Height of Large/Small PM Rings (mm) A	Radial Length of Large/Small PM Rings (mm) B	Height of Coils (mm) C
1	10.5	10	5.5
2	11.5	11	9.5
3	12.5	12	12.5

Table 2. L_9 ($3^2 \times 3^2$) size optimization simulations of the actuator by the orthogonal experiment method.

Number	Height of Large/Small PM Rings (mm)	Radial Length of Large/Small PM Rings (mm)	Height of Coils (mm)	Magnetic Force (N)
1	A1	B1	C1	156
2	A1	B2	C2	171
3	A1	B3	C3	156
4	A2	B1	C2	135
5	A2	B2	C3	159
6	A2	B3	C1	171
7	A3	B1	C3	165
8	A3	B2	C1	150
9	A3	B3	C2	180

The analysis by the orthogonal experiment method (L_9 ($3^2 \times 3^2$) size) is shown in Table 3. As can be observed, the combination (A3B3C2) is the optimal parameters, which are the height of large/small PM rings (12.5 mm), the radial length of large/small PM rings (12 mm), and the height of coils (9.5 mm).

Table 3. Analysis by the orthogonal experiment method.

Value Name	Height of $Coil_2$ (mm)	Thickness of $Coil_2$ (mm)	Height of Soft $Iron\ Ring_1$ (mm)
K_{j1}	543	516	537
K_{j2}	525	540	546
K_{j3}	555	567	540
K_{jp1}	181	172	179
K_{jp2}	175	180	182
K_{jp3}	185	189	180
R_j	10	17	3
Primary and secondary order		B > A > C	
Optimal levels	A3	B3	C2
Optimal combination		A3B3C2	

Note: K_{jk} (k = 1, 2, 3) is the sum of the simulation results with the same level k in the j^{th} column. K_{jpk} is the mean value of the simulation results with the same level k in the j^{th} column. R_j is the range of K_{jpk}.

2.2. Sizes and Principles of the Electromagnetic Actuator

According to Section 2.1, the dimension mark and magnetic flux in the air gap are as shown in Figure 3. Figure 3a,b, respectively, show sectional views in the radial direction and in the axial direction. The magnetic flux is emitted from the N pole of the small PM rings through the air gap, the coils, and the coil bobbin. Then, it is gathered at the S level of the large PM ring. This structure for dual PM rings can generate magnetic flux in the same direction as the air gap, which is equivalent to increasing the magnetic focusing effect. Six groups of the dual PM rings generate magnetic flux in the same direction within the air gap. When the coils move in the axial direction, they cause as much magnetic flux as possible. The size parameters of the electromagnetic actuator are shown in Table 4.

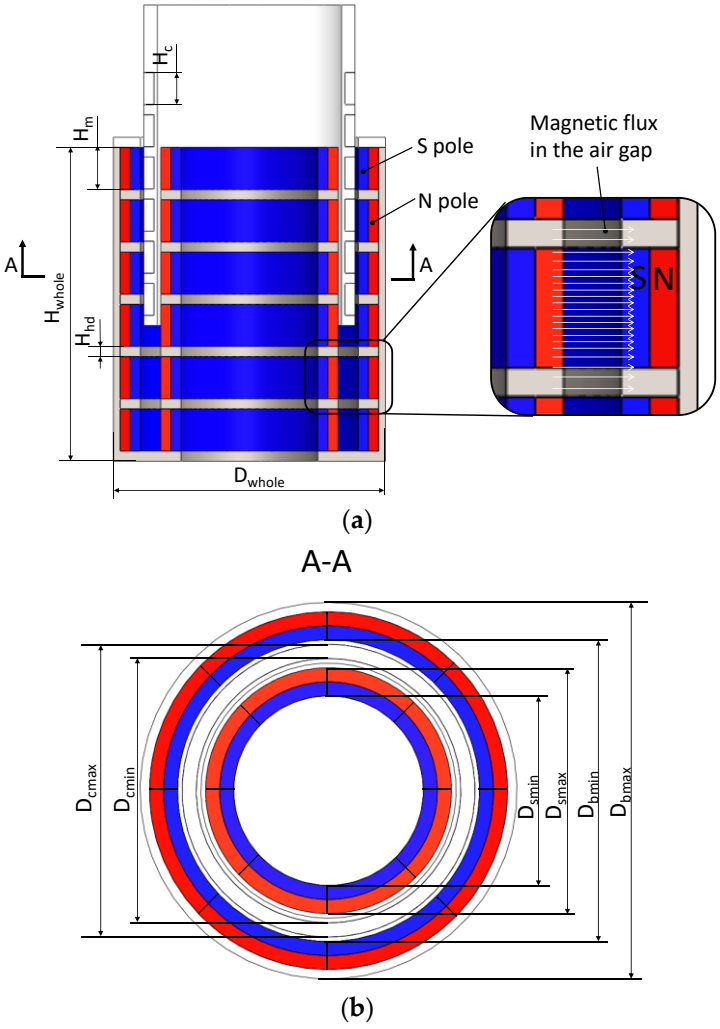

Figure 3. Dimensional drawing. (**a**) Sectional view in the radial direction. (**b**) Sectional view in the axial direction.

Table 4. Size parameters of the electromagnetic actuator.

Size Parameter	Description	Value (Unit: mm)
H_c	Axial length of the coils	9.5
H_m	Axial length of the PM ring	12.5
H_{hd}	Axial length of the heat-dissipated ring	3
H_{whole}	Axial length of the actuator	96
D_{whole}	Outside diameter of the actuator	80.6
D_{cmax}	Outside diameter of the coils	62.3
D_{cmin}	Inside diameter of the coils	56.6
D_{smax}	Outside diameter of the small PM rings	52.6
D_{smin}	Inside diameter of the small PM rings	40.6
D_{bmax}	Outside diameter of the large PM rings	76.6
D_{bmin}	Inside diameter of the large PM rings	64.6

3. Model and Analysis of the Magnetic Field

In the electromagnetic actuator, the magnetic field in the air gap of the stator is the main factor for improving performance. The homogeneity of the magnetic field in the air gap along the actuator's axial direction decides the stability and linearity of the actuator's thrust force. The magnetic flux density in the air gap decides the thrust force of an actuator and the ride comfort of a vehicle. First, the model of the magnetic flux density in an air gap is built, and the characteristic of the magnetic field is theoretically analyzed.

3.1. Magnetic Flux Density Model of a Single PM Ring

To analyze the quasi-parallel magnetic field in the air gap between the PM ring arrays and the inner wall of the actuator, the mathematical model of the magnetic flux density of the magnet field is built in the y direction according to the Ampere molecular circulation hypothesis, as shown in Figure 4. When the positive direction of the magnet field is $+y$ direction, the spatial magnetic field is equivalent to the magnetic field generated by Surface Currents 1 and 2 [36,37].

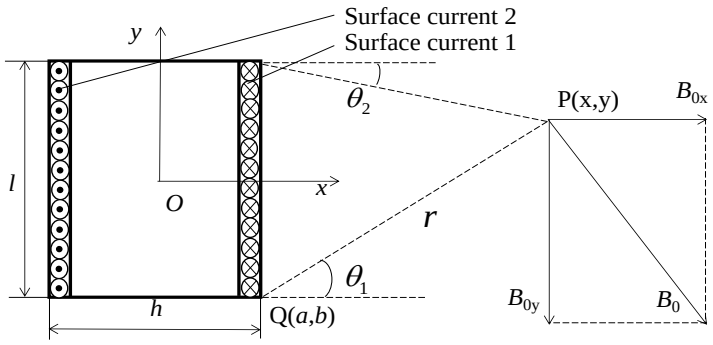

Figure 4. Schematic diagram of the magnetic field of a single PM ring.

A schematic diagram of the magnetic field of a single PM ring is shown in Figure 4. The description of the variables in the formulas is shown in Table 5. The magnetic flux density formula at point P(x, y) in the y direction can be expressed as follows [38–40]:

$$B_{\mathrm{oy}} = -B_o \cos\theta \tag{1}$$

where

$$B_{\mathrm{o}} = \frac{\mu_0 k_{\mathrm{v}}}{2\pi r};\ \theta = \arcsin\left(\frac{y-b}{r}\right)$$

The magnetic flux density B_{y11} and B_{y12} generated by the surface currents 1 and 2 can be expressed as (2) and (3) [41–43]:

$$\begin{aligned} B_{y11} &= \int_{\theta_1}^{\theta_2} \frac{\mu_0 k_v}{2\pi r} \sin\theta \, \mathrm{d}b \\ &= \frac{\mu_0 k_v}{2\pi} [\arctan(\frac{y-l/2}{x-h/2}) - \arctan(\frac{y+l/2}{x-h/2})] \end{aligned} \tag{2}$$

$$\begin{aligned} B_{y12} &= -\int_{\theta_1}^{\theta_2} \frac{\mu_0 k_v}{2\pi r} \cos\theta \, \mathrm{d}b \\ &= \frac{\mu_0 k_v}{2\pi} [\arctan(\frac{y+l/2}{x+h/2}) - \arctan(\frac{y-l/2}{x+h/2})] \end{aligned} \tag{3}$$

where

$$r = \frac{x-h/2}{\cos\theta} \qquad db = -\frac{x-h/2}{(\cos\theta)^2} d\theta$$
$$\theta_1 = \arctan\left(\frac{y+l/2}{x-h/2}\right) \quad \theta_2 = \arctan\left(\frac{y-l/2}{x-h/2}\right)$$

Table 5. Variable table.

Variable	Description
$Q(a, b)$	Horizontal and vertical coordinates of any current source
$P(x, y)$	Horizontal and vertical coordinates of any point in a plane
j	Ring number from left to right, j = 1–6
θ_1, θ_2	Angle between the upper and lower points of surface current 1
θ	Angle between the line of point Q and point P and the horizontal line
r	Distance between point Q and point P
B_{yj1}	Magnetic flux density of surface current 1
B_{yj2}	Magnetic flux density of surface current 2
B_{y1}	Magnetic flux density of large PM rings
B_{y2}	Magnetic flux density of small PM rings
B_y	Magnetic flux density of the PM ring array

3.2. Magnetic Flux Density Model of the Magnet Assembly

To analyze the magnetic fields of two groups of PM ring arrays, the magnetic flux density of the PM ring array B_y in the air gap can be expressed as (4) [43]:

$$\begin{aligned} B_y &= B_{y1} + B_{y2} \\ B_{yj} &= \sum_{i=1}^{6} B_{yj1} + \sum_{i=1}^{6} B_{yj2} \end{aligned} \tag{4}$$

$$B_{yj1} = \frac{\mu_0 k_v}{2\pi} \arctan\left(\frac{y - l/2}{x - (j-1)\cdot(h+s) - h/2}\right) - \frac{\mu_0 k_v}{2\pi} \arctan\left(\frac{y + l/2}{x - (j-1)\cdot(h+s) - h/2}\right) \tag{5}$$

$$B_{yj2} = \frac{\mu_0 k_v}{2\pi} \arctan\left(\frac{y + l/2}{x - (j-1)\cdot(h+s) + h/2}\right) - \frac{\mu_0 k_v}{2\pi} \arctan\left(\frac{y - l/2}{x - (j-1)\cdot(h+s) + h/2}\right) \tag{6}$$

3.3. Theoretical Analysis of Magnetic Flux Density

According to the magnetic flux density model of the actuator's magnet assembly, the magnetic flux density was calculated by (4) in the middle of the air gap and along the whole axial length of 90 mm. The calculated results of the magnetic flux density of each PM ring and the superimposed magnetic flux density of the six PM ring arrays are shown in Figure 5. The results of each PM ring are shown as a normal distribution curve, the superimposed magnetic flux density B_y is shown as regular fluctuations, and its value varies between 51.73 and 788.49 mT.

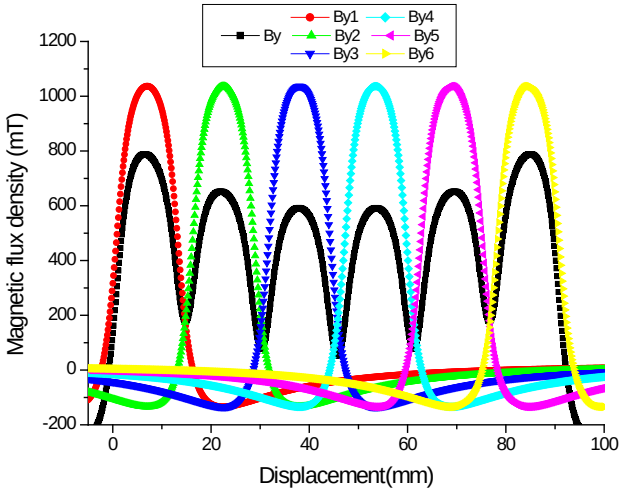

Figure 5. Theoretical results of magnetic flux density.

4. FEM Analysis of the Magnetic Field

4.1. FEM Analysis Model

To compare with the magnetic field theory model, a 2-D FEM analysis on the magnetic field and magnetic flux density was conducted using a magnetic field analysis software program. A half 2-D FEM model was built with the same dimension parameters as in Table 4, since the structure of the actuator is axisymmetric. In the FEM model, the remanence Br of the permanent magnet was 1.38–1.44 T, and the coercivity was −876 KA/m.

4.2. FEM Analysis on the Magnetic Field

Based on the cylinder coordinate system, the electromagnetic actuator is simulated to obtain the magnetic density and magnetic flux trend by FEM. The simulation adopts a cylindrical coordinate system. The axle of the actuator is *z*-axis, shown in Figure 6, and the same graphical scales of 0–100 mm are used. The result of the FEM analysis clarifies the characteristics of the quasi-parallel magnetic field for the actuator using PM ring arrays. Since the S pole of the large PM rings is parallel to the N pole of the small PM rings in the air gap of the electromagnetic actuator, there is less magnetic flux leakage. The magnetic flux is nearly parallel in the air gap and its distribution is relatively even in the air gap except for the two ends. This proves that when it moves in the air gap, the coil moves through, cutting the parallel magnetic flux.

Assumption: Each coil has a diameter of 1 mm and a current of 0.8 A is applied. After applying direct current to each coil, the eddy current loss in the simulation is approximately 3 W. Figure 6 shows the simulation structure of the electromagnetic actuator at 0.04 s.

Figure 6a shows the FEM simulation results for the magnetic flux density. From the legend on the left, the magnetic flux density ranges from 4.9979×10^{-3} T to 2.500 T. From the magnetic flux density results in the radial direction, it can be seen that the magnetic flux density in the air gap between the large PM rings and the small PM rings is about 550 mT, and the magnetic flux density at both ends is about 670 mT. The magnetic flux density of the large and small heat-dissipated rings is about 1.9 T. The magnetic flux density of the heat-dissipated rings in the middle of the same-size PM rings in the axial direction is relatively large.

Figure 6b shows the FEM simulation results in the direction of magnetic flux. From the legend on the left, the magnetic flux density for the direction of magnetic flux ranges from 4.9979×10^{-3} T to 2.500 T, which is the same as in Figure 6a. The results show that the magnetic flux between the large PM rings and the small PM rings is perpendicular to the axial direction of the electromagnetic actuator, and the directions of the multiple magnetic fluxes are parallel to each other. There will be divergence at the edge of each PM ring. Therefore, a magnetic field will be generated at the heat-dissipated rings. In theoretical calculations, the edge effects of the PM rings are assumed to be 0 mT, and this is reflected in the FEM simulation.

Figure 6c shows the FEM simulation results of the magnetic flux trend. From the legend on the left, the magnetic flux distribution for the magnetic flux trend ranges from -2.214×10^{-4} T to 2.024×10^{-4} T. The results show that the parallel magnetic field between the large PM rings and the small PM rings is visible, and the magnetic flux in the large heat-dissipated rings and the small heat-dissipated rings is repulsive; in the simulation boundary, due to the inevitable phenomenon of magnetic leakage, the magnetic flux must exist outside the electromagnetic actuator.

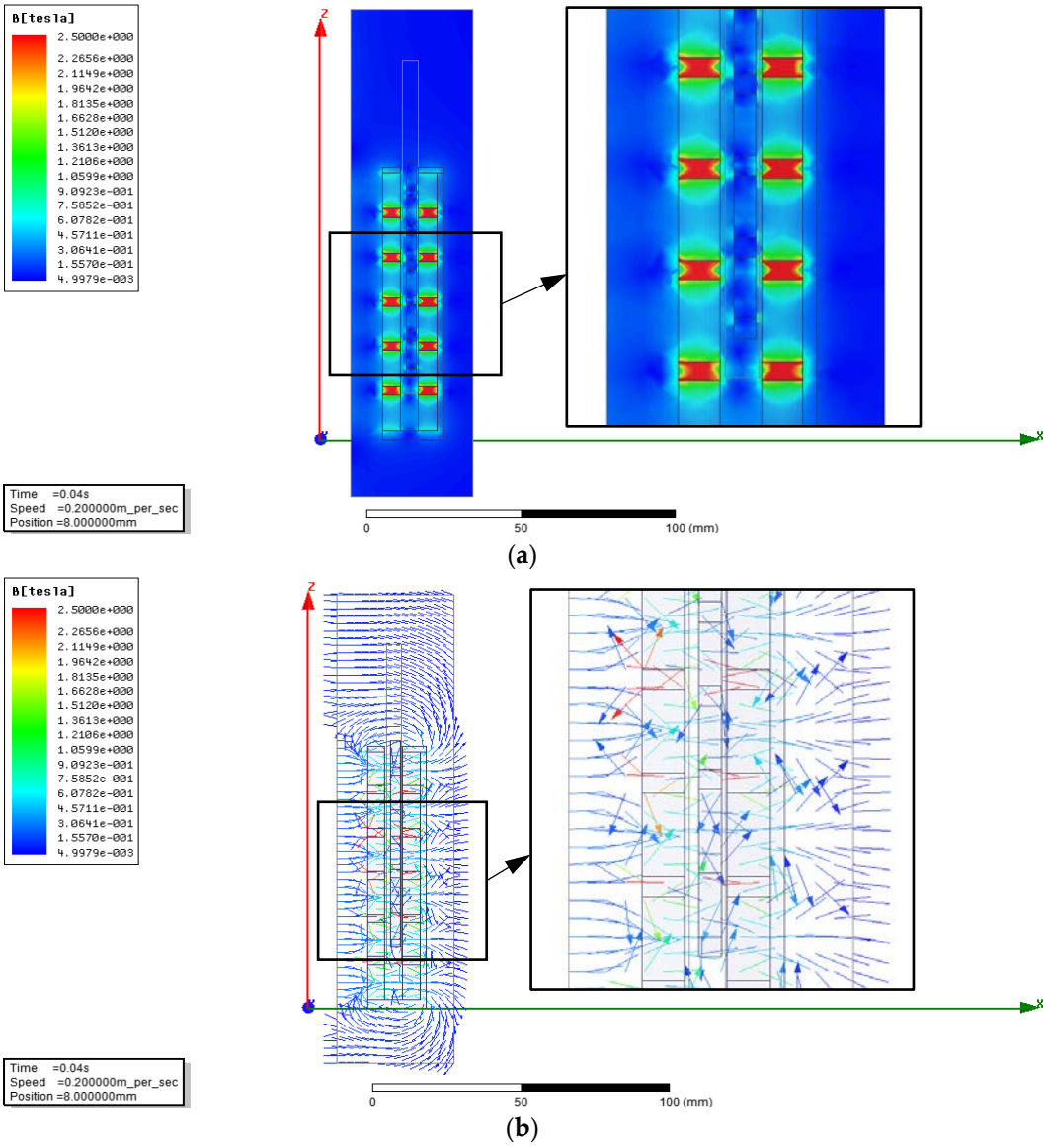

Figure 6. *Cont.*

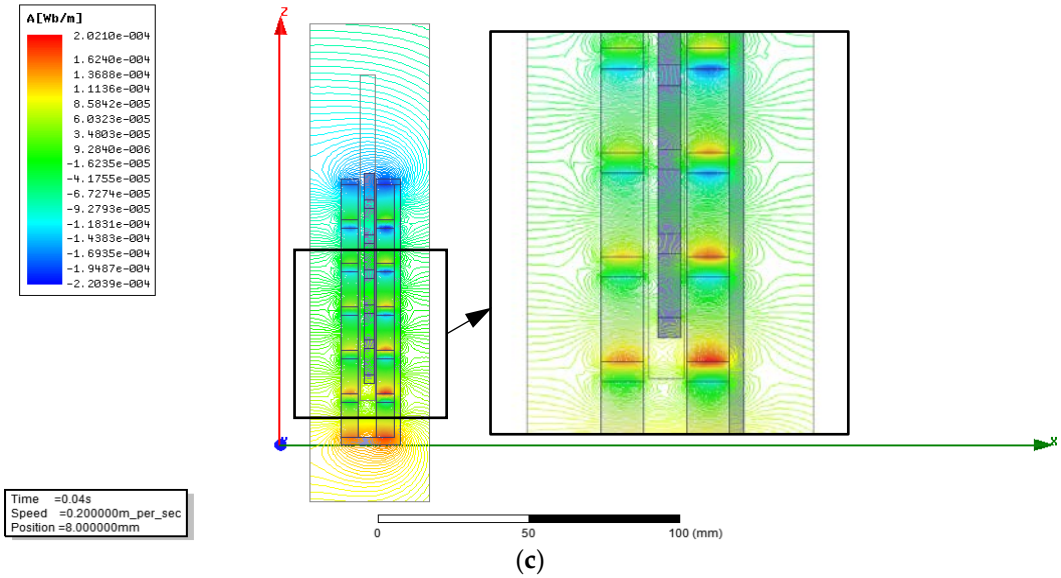

Figure 6. FEM analysis of magnetic field for half of the actuator. (**a**) The magnetic flux density. (**b**) The direction of magnetic flux. (**c**) The trend of magnetic flux.

4.3. FEM Analysis of the Magnetic Flux Density

To compare with the theoretical results of the magnetic field model, the superimposed magnetic flux density of the magnet assembly was also analyzed using the 2-D FEM model. The FEM analysis results in Figure 7 clarify the characteristics of the quasi-parallel magnetic field for the magnet assembly using PM ring arrays. The positions of the axial air gap of the PM ring arrays were analyzed, which is the same as the theoretical calculation positions.

Curve By is the magnetic flux density of the PM ring arrays in the axial air gap. Curve By1 to curve By6 are the magnetic flux densities of six magnetic rings from the lower to upper cover. In an air gap magnetic field, the magnetic flux density is roughly in the range of 100 mT–650 mT. Compared to the theoretical result curves, these curves roughly exhibit an irregular sinusoidal shape. At the axial center of the permanent magnet, the magnetic flux density is the highest. At the axial center of the heat-dissipation ring, the magnetic flux density is the smallest. The theoretical calculation curve trend is consistent with the FEM simulation curve trend, with a slightly lower peak magnetic flux density at the middle magnetic rings. The irregular shape of the curve may be due to the consideration of eddy current losses, edge effects of magnets, and other factors in the FEM simulation.

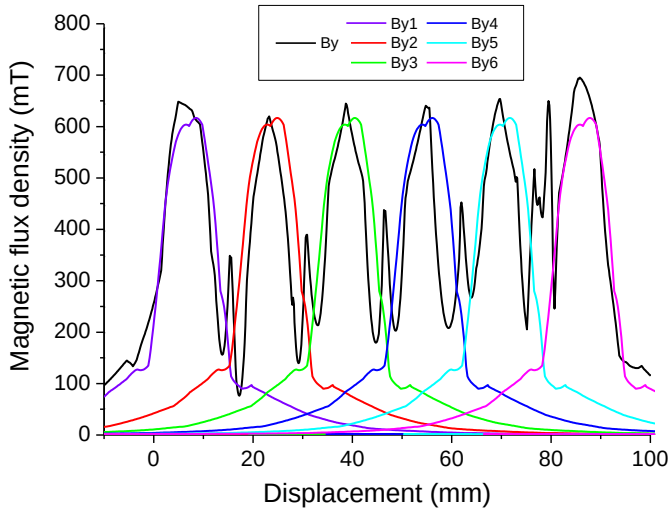

Figure 7. Simulation results of magnetic flux density.

To verify the curve trend of theoretical results and finite element results, the PM arrangement in [44] is similar to that used in this paper. Reference [44] studied an electromagnetic actuator for an active suspension (as shown in Figure 3 of [44]), which uses a single-layer magnetic ring array. The arrangement of magnetic poles is that the outer side is N pole, the inner side is S pole, and each magnetic ring is composed of eight same pieces. The magnetic flux (as shown in Figure 3 of [44]) is emitted from the N pole of the PM rings, passes through the air gap, the outer and inner walls, and then returns to the S pole of the PM rings. This paper adopts a double-layer magnetic ring array, in which the N poles of the small magnetic rings are in face of the S poles of the large magnetic rings in the air gap. Each magnetic ring is also composed of eight same pieces.

In the air gap, compared with the magnet ring array (as shown in Figure 6 of [44]), adding a layer of magnetic ring array will increase the magnetic flux density of the air gap. The theoretical and finite element results of the magnetic ring array are compared and analyzed with the experimental results, as shown in Figure 8. The magnetic field trends of the three curves are consistent, and each curve owns six peaks at the same position. This can prove the correctness of the magnetic flux density trend of the theoretical model derived in this paper. Due to the same position of six peaks, the magnetic flux density will increase as the volume of the magnet rings increases. The experimental results of magnetic field density in [44] are approximately in the range of 50–200 mT, and the theoretical and simulation results of magnetic field intensity in this paper are approximately in the range of 100–650 mT. Therefore, the arrangement of the magnet ring array in this paper with a large magnetic flux density in the air gap is superior to that in [44].

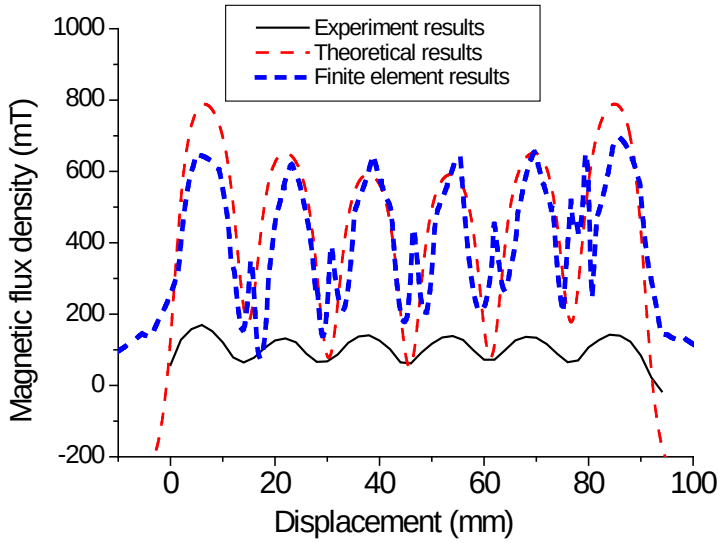

Figure 8. Three results of magnetic flux density.

4.4. FEM Analysis on Magnetic Force

Based on the magnetic field characteristics of the electromagnetic actuator, it is necessary to analyze the magnetic force characteristics of the electromagnetic actuator, as shown in Figure 9. The magnetic force characteristics are divided into the current–magnetic force characteristics and the displacement–magnetic force characteristics.

The current–magnetic force curve is shown in Figure 9a. The current range is −1.8 A to 1.8 A, and the magnetic force range of the electromagnetic actuator is −219.8 N to 220.9 N. The current–magnetic force characteristic curve passes through the origin [0,0]. When the current is 1 A, the magnetic force is 122.2 N. When the current is −1 A, the magnetic force is −122.0 N. The slope of the current force curve is approximately 122.2.

The displacement–magnetic force curve is shown in Figure 9b, which is the displacement–magnetic force curve when the current is 0.5 A, 1.0 A, and 1.5 A, respectively. With increasing

displacement, the magnetic attenuation is 0.187 N/mm. When the current is 1.0 A and 1.5 A, the magnetic attenuation is 0.376 N/mm and 0.618 N/mm, respectively.

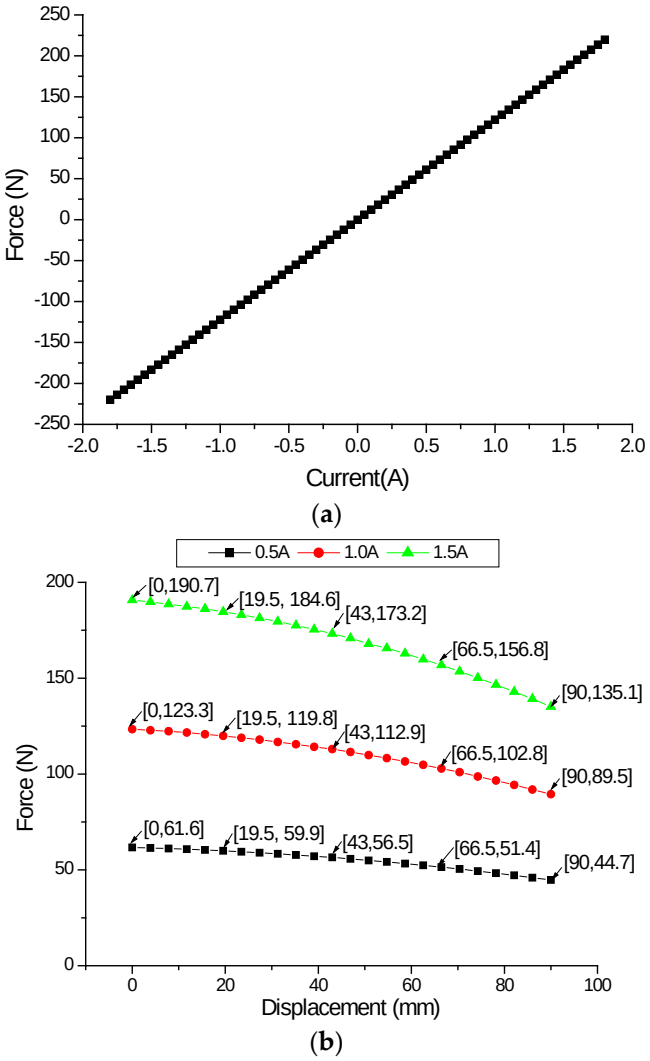

Figure 9. Simulation results of magnetic force characteristics. (**a**) The current–magnetic force curve. (**b**) The displacement–magnetic force curve.

5. Vehicle Simulation Based on the Fuzzy PID Algorithm

To obtain the dynamic characteristics of the electromagnetic suspension, a seven-DOF dynamics model of the whole vehicle was established, and then the fuzzy PID simulation analysis was carried out.

5.1. Vehicle Dynamics Model

The pitch and roll characteristics of the whole vehicle are analyzed through the seven DOF dynamics model. The seven-DOF dynamics model based on fuzzy PID control is shown in Figure 10, and its parameters and descriptions are shown in Table 6. Based on the dynamics model of the passive suspension of the whole vehicle, electromagnetic suspension actuators are introduced at the four shock absorbers, and the magnetic forces F_{iA}, F_{iB}, F_{iC}, and F_{iD} are generated.

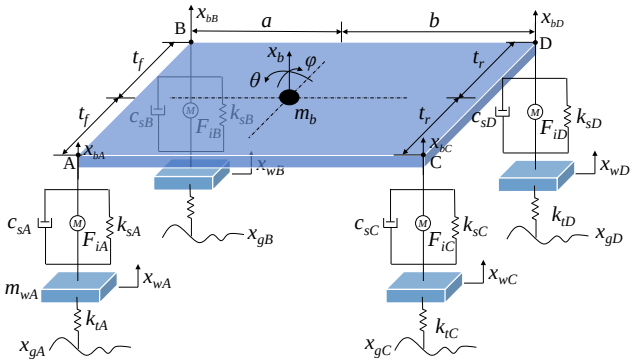

Figure 10. Seven-DOF dynamics model based on fuzzy PID control.

Table 6. Variable table for seven-degree-of-freedom vehicle suspension.

Variable	Description
x_b	Displacement of body centroid
m_b	Mass of body centroid
θ	Pitch angle
φ	Roll angle
a	Distance from the center of mass to the front axle
b	Distance from the center of mass to the rear axle
t_f	1/2 front track
t_r	1/2 rear track
m_{wA}	Mass of the left front wheel
m_{wB}	Mass of the right front wheel
m_{wC}	Mass of the left rear wheel
m_{wD}	Mass of the right rear wheel
x_{wA}	Displacement of the left front wheel
x_{wB}	Displacement of the right front wheel
x_{wC}	Displacement of the left rear wheel
x_{wD}	Displacement of the right rear wheel
k_{tA}	Stiffness of the left front wheel
k_{tB}	Stiffness of the right front wheel
k_{tC}	Stiffness of the left rear wheel
k_{tD}	Stiffness of the right rear wheel
k_{sA}	Stiffness of the left front wheel spring
k_{sB}	Stiffness of the right front wheel spring
k_{sC}	Stiffness of the left rear wheel
k_{sD}	Stiffness of the right rear wheel
c_{sA}	Left front wheel damping coefficient
c_{sB}	Right front wheel damping coefficient
c_{sC}	Left rear wheel damping coefficient
c_{sD}	Right rear wheel damping coefficient
x_{gA}	Left front wheel road displacement
x_{gB}	Right front wheel road displacement
x_{gC}	Left rear wheel road displacement
x_{gD}	Right rear wheel road displacement
x_{bA}	Left front wheel spring mass displacement
x_{bB}	Right front wheel spring mass displacement
x_{bC}	Left rear wheel sprung mass displacement
x_{bD}	Right rear wheel sprung mass displacement

According to the dynamics model of the whole vehicle with seven DOF, the dynamics model of the whole suspension system is established using Newton's law. The seven DOF are centroid acceleration, pitch angle acceleration, roll angle acceleration, and vertical displacements of four wheels. Then, the vertical displacements of the four wheels can be expressed by Equations (7)–(10), and the centroid acceleration, pitch angle acceleration, and roll angle acceleration can be expressed by Equations (11)–(13), respectively. The seven-DOF dynamics model is as follows, and the physical quantities in Equations (7)–(13) can be seen in Figure 10.

$$m_{wA}\ddot{x}_{wA} = k_{tA}(x_{gA} - x_{wA}) + k_{sA}(x_{bA} - x_{wA}) + c_{sA}(\dot{x}_{bA} - \dot{x}_{wA}) + F_{iA} \tag{7}$$

$$m_{wB}\ddot{x}_{wB} = k_{tB}(x_{gB} - x_{wB}) + k_{sB}(x_{bB} - x_{wB}) + c_{sB}(\dot{x}_{bB} - \dot{x}_{wB}) + F_{iB} \tag{8}$$

$$m_{wC}\ddot{x}_{wC} = k_{tC}(x_{gC} - x_{wC}) + k_{sC}(x_{bC} - x_{wC}) + c_{sC}(\dot{x}_{bC} - \dot{x}_{wC}) + F_{iC} \tag{9}$$

$$m_{wD}\ddot{x}_{wD} = k_{tD}(x_{gD} - x_{wD}) + k_{sD}(x_{bD} - x_{wD}) + c_{sD}(\dot{x}_{bD} - \dot{x}_{wD}) + F_{iD} \tag{10}$$

$$\begin{aligned} m_b\ddot{x}_b = {} & c_{sA}(\dot{x}_{wA} - \dot{x}_{bA}) + k_{sA}(x_{wA} - x_{bA}) + c_{sB}(\dot{x}_{wB} - \dot{x}_{bB}) + k_{sB}(x_{wB} - x_{bB}) + c_{sC}(\dot{x}_{wC} - \dot{x}_{bC}) \\ & + k_{sC}(x_{wC} - x_{bC}) + c_{sD}(\dot{x}_{wD} - \dot{x}_{bD}) + k_{sD}(x_{wD} - x_{bD}) + F_{iA} + F_{iB} + F_{iC} + F_{iD} \end{aligned} \tag{11}$$

$$\begin{aligned} I_p\ddot{\theta} = {} & [c_{sC}(\dot{x}_{wC} - \dot{x}_{bC}) + k_{sC}(x_{wC} - x_{bC}) + F_{iC} + c_{sD}(\dot{x}_{wD} - \dot{x}_{bD}) + k_{sD}(x_{wD} - x_{bD}) + F_{iD}] \cdot b \\ & - [c_{sA}(\dot{x}_{wA} - \dot{x}_{bA}) + k_{sA}(x_{wA} - x_{bA}) + F_{iA} + c_{sB}(\dot{x}_{wB} - \dot{x}_{bB}) + k_{sB}(x_{wB} - x_{bB}) + F_{iB}] \cdot a \end{aligned} \tag{12}$$

$$\begin{aligned} I_r\ddot{\varphi} = {} & [c_{sA}(\dot{x}_{wA} - \dot{x}_{bA}) + k_{sA}(x_{wA} - x_{bA}) + F_{iA} - c_{sB}(\dot{x}_{wB} - \dot{x}_{bB}) - k_{sB}(x_{wB} - x_{bB}) - F_{iB}] \cdot t_f \\ & + [c_{sC}(\dot{x}_{wC} - \dot{x}_{bC}) + k_{sC}(x_{wC} - x_{bC}) + F_{iC} - c_{sD}(\dot{x}_{wD} - \dot{x}_{bD}) - k_{sD}(x_{wD} - x_{bD}) - F_{iD}] \cdot t_r \end{aligned} \tag{13}$$

where

$$\begin{aligned} x_{bA} &= x_b - a \cdot \theta + t_f \cdot \varphi \quad F_{iA} = k_{iA} \cdot I_A \\ x_{bB} &= x_b - a \cdot \theta - t_f \cdot \varphi \quad F_{iB} = k_{iB} \cdot I_B \\ x_{bC} &= x_b + b \cdot \theta + t_r \cdot \varphi \quad F_{iC} = k_{iC} \cdot I_C \\ x_{bD} &= x_b + b \cdot \theta - t_r \cdot \varphi \quad F_{iD} = k_{iD} \cdot I_D \end{aligned}$$

Vehicle parameters are shown in Table 7.

Table 7. Vehicle parameters.

Parameters (Unit)	Value	Parameters (Unit)	Value
m_s (kg)	1836	c_{sA} (N/(m/s))	1800
m_{wA} (kg)	50	c_{sB} (N/(m/s))	1800
m_{wB} (kg)	50	c_{sC} (N/(m/s))	2000
m_{wC} (kg)	50	c_{sD} (N/(m/s))	2000
m_{wD} (kg)	50	k_{tA} (N/m)	230,000
I_p (kg·m^2)	3411	k_{tB} (N/m)	230,000
I_r (kg·m^2)	676	k_{tC} (N/m)	230,000
k_{sA} (N/m)	57,000	k_{tD} (N/m)	230,000
k_{sB} (N/m)	57,000	a (m)	1.455
k_{sC} (N/m)	64,000	b (m)	1.514
k_{sD} (N/m)	64,000	t_l (m)/t_r (m)	0.805

5.2. Fuzzy PID Control Algorithm

The fuzzy PID control block diagram is shown in Figure 11. The external disturbance of the vehicle suspension system is road excitation. The centroid acceleration is set to 0 mm/s^2, and the input of the fuzzy controller is the deviation e and the variation of the deviation ec. Based on fuzzy control rules, PID parameters are adjusted online to meet different requirements for PID parameters with different deviations e and incremental deviations ec. The simulation employs a variable-step solver with a maximum sampling step of 0.01 s, utilizing the Ode45 solver algorithm. The simulation is set to run for a duration of 5 s. The actives of the simulation are centroid acceleration, acceleration of the roll angle, acceleration of the pitch angle, dynamic deflections for four wheels, and dynamic loads for four wheels.

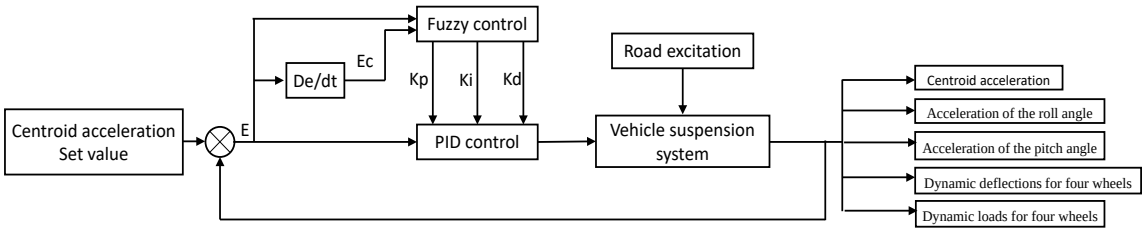

Figure 11. Fuzzy PID control block diagram.

5.3. Vehicle Simulation Results Based on Fuzzy PID under C-Grade Surface

Based on Matlab/Simulink simulation software, the fuzzy PID control simulation analysis of electromagnetic suspension is carried out and compared with the passive suspension. Three evaluation indicators of vehicle ride comfort are analyzed, namely body acceleration, roll angle, and pitch angle. Take the C-grade road surface (as shown in Figure 12) as the input road surface and set the vehicle speed to 20 km/h. The fuzzy PID simulation parameters are adjusted and determined by the parameter setting method. Therefore, the fuzzy PID control law is shown in Table 8. The PID control parameters are $k_p = 1$, $k_i = 20$, and $k_d = 0.01$.

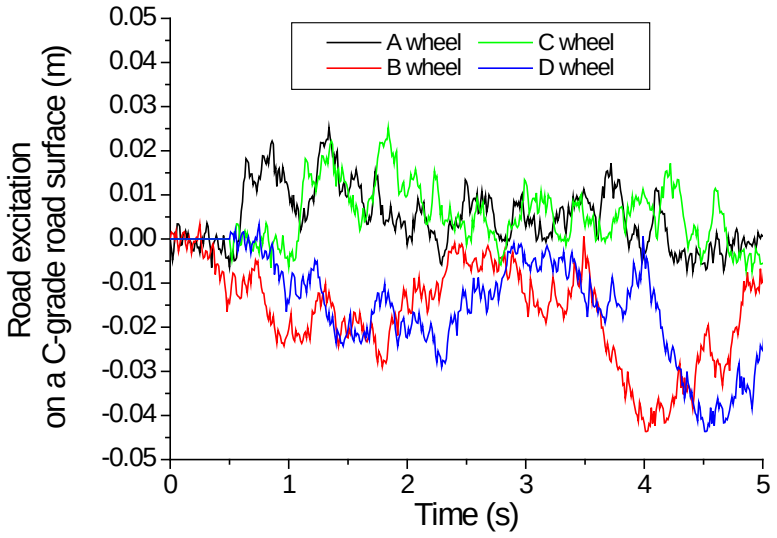

Figure 12. Road excitation on a C-grade road surface for four wheels.

The simulation results of centroid acceleration, acceleration of the roll angle, and acceleration of the pitch angle based on the fuzzy PID controller are shown in Figures 13–15, which show the simulation comparison results of three main evaluation indicators. The trend of active suspension and passive suspension of the three curves is the same. The root mean square (RMS) values of the centroid acceleration, acceleration of the roll angle, and

acceleration of the pitch angle are 59.08%, 3.06%, and 3.54% higher than those of passive suspension, respectively. The tracking response of these three curves is fast.

In the simulation results of vehicle body acceleration in Figure 13, there is a slight delay, with a delay time of 0.05 s. The acceleration of roll angle curve is shown in Figure 14. At 3 s, the peak value of the electromagnetic suspension is 0.012 rad/s^2 less than that of the passive suspension. The acceleration of the pitch angle curve is shown in Figure 15. At 1.96 s, the maximum value of the electromagnetic suspension is 0.153 rad/s^2 less than that of the passive suspension.

Table 8. Control law on C-grade road surface for fuzzy PID algorithm.

U		Ec						
		NB	**NM**	**NS**	**Z**	**PS**	**PM**	**PB**
E	NB	PB	PB	PM	PM	PS	Z	Z
	NM	PB	PB	PM	PS	PS	Z	NS
	NS	PM	PM	PS	PS	Z	NS	NS
	Z	PM	PM	PS	Z	NS	NM	NM
	PS	PS	PS	Z	NS	NS	NM	NM
	PM	PS	Z	NS	NM	NM	NM	NB
	PB	Z	Z	NM	NM	NM	NB	NB

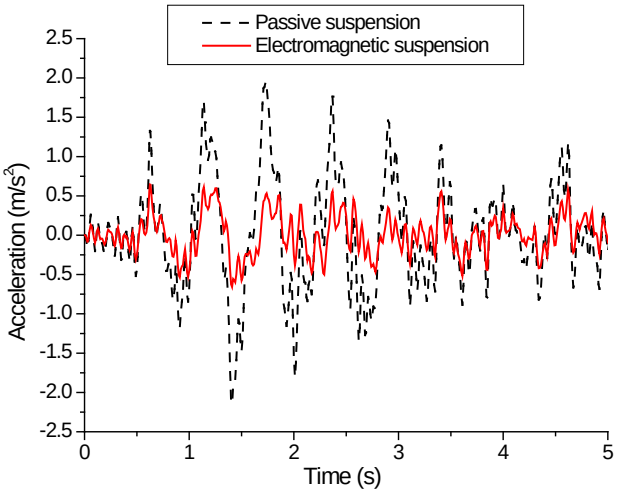

Figure 13. Centroid acceleration on a C-grade road surface.

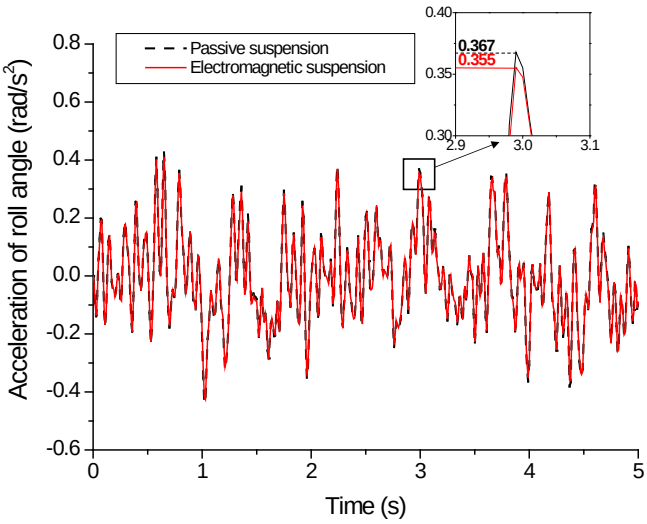

Figure 14. Acceleration of the roll angle on a C-grade road surface.

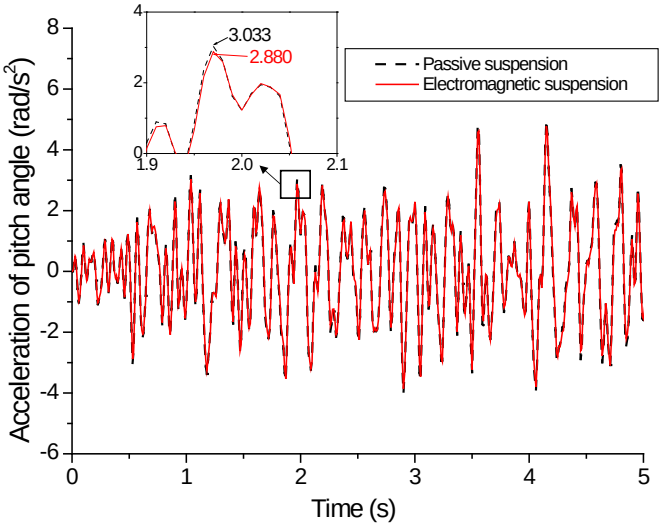

Figure 15. Acceleration of the pitch angle on a C-grade road surface.

The simulation results of the dynamic deflections for the four wheels are shown in Figure 16. The simulation results of the suspension's dynamic deflection for wheels A, B, C, and D are analyzed. The simulation results show that the maximum dynamic deflections of the electromagnetic active suspension are slightly lower than those of the passive suspension, and the controller has good tracking performance. The suspension dynamic deflections of wheels A, B, C, and D are 13.20%, 9.84%, 11.98%, and 16.42%, respectively, which are lower than the corresponding root mean square (RMS) value of the passive suspension.

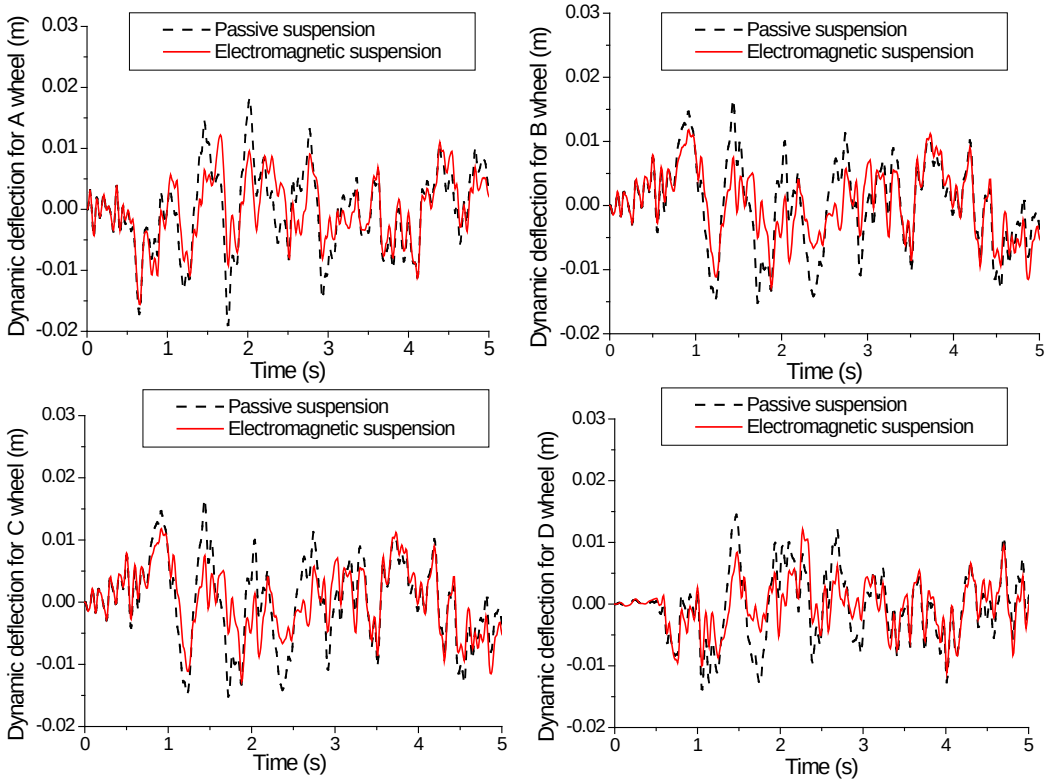

Figure 16. Dynamic deflections on a C-grade road surface for four wheels.

The simulation results of the dynamic load for four wheels are shown in Figure 17. The dynamic load is closely related to the tire operation life and the impact of road damage. The simulation results show that the dynamic load of the four wheels of the electromagnetic suspension is less than the dynamic load of the passive suspension, which can reduce the impact of the tire on the road and the wear of the tire itself. The dynamic loads of the tires for the electromagnetic suspension show partial attenuation near each peak. The RMS values of the dynamic loads of wheels A, B, C, and D are 2.87%, 1.42%, 2.09%, and 5.04% lower than those of the passive suspension, respectively.

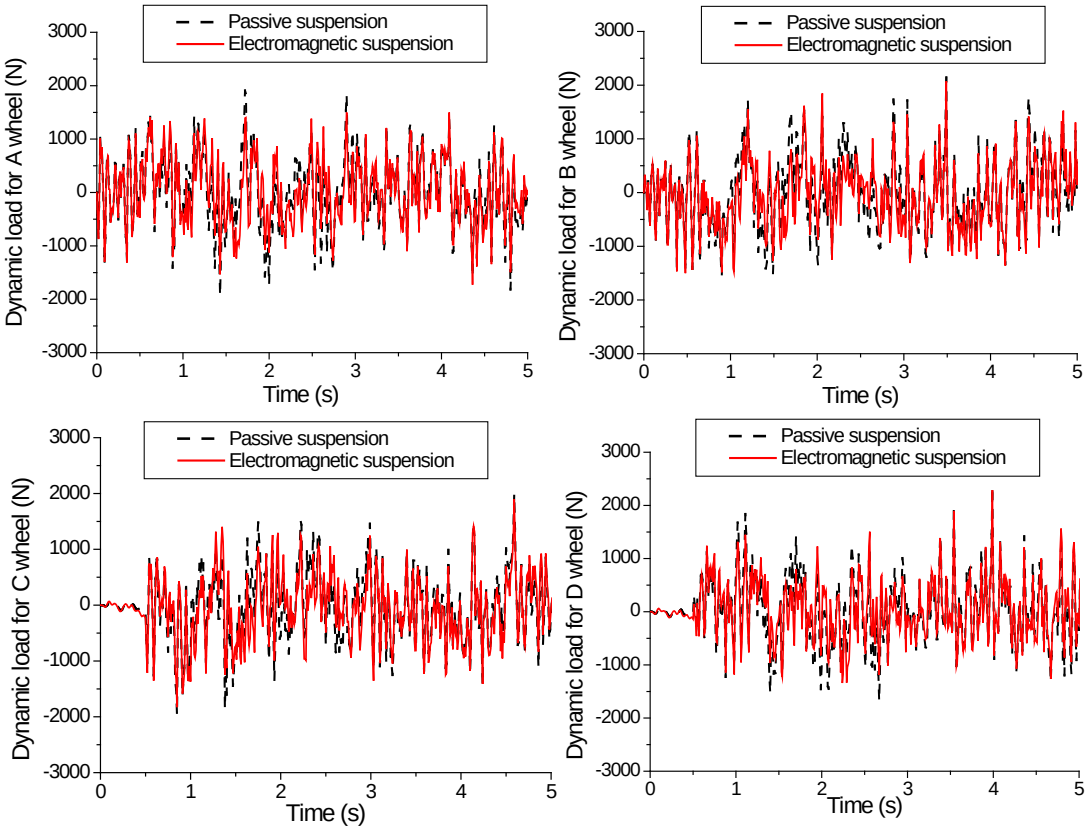

Figure 17. Dynamic loads on a C-grade road surface for four wheels.

5.4. Vehicle Simulation Results Based on Fuzzy PID under a Deceleration Strip Surface

Based on the simulation on a C-level road surface in Section 5.3, a road excitation with a deceleration strip is introduced as shown in Figure 18. The deceleration strip adopts a trapezoidal shape with an upper edge of 200 mm, a lower edge of 400 mm, and a height of 30 mm. A fuzzy PID control simulation analysis was conducted on the electromagnetic suspension and compared with the passive suspension with a vehicle speed of 20 km/h. The fuzzy PID simulation parameters are adjusted and determined by setting the parameters. The fuzzy PID control law is shown in Table 9. The PID control parameters are k_p = 0.8, k_i = 50, and k_d = 0.001. This simulation analysis can provide a detailed analysis of the pitch and roll characteristics to showcase the advantages of the electromagnetic suspension.

Table 9. Control law with a deceleration strip for fuzzy PID algorithm.

U		Ec						
		NB	**NM**	**NS**	**Z**	**PS**	**PM**	**PB**
E	NB	PB	PB	PM	PM	PS	Z	Z
	NM	PB	PB	PM	PS	PS	Z	NS
	NS	PM	PM	PS	PS	Z	NS	NS
	Z	PM	PM	PS	Z	NS	NM	NM
	PS	PS	PS	Z	NS	NS	NM	NM
	PM	PS	Z	NS	NS	NM	NB	NB
	PB	Z	Z	NM	NM	NM	NB	NB

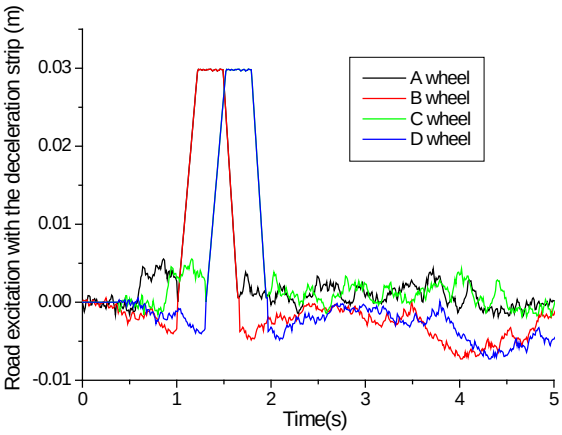

Figure 18. Road excitation with the C deceleration strip for four wheels.

The simulation results of the centroid acceleration, acceleration of the roll angle, and acceleration of the pitch angle based on a fuzzy PID controller are shown in Figures 19–21, which show the simulation comparison results of the three main evaluation indicators. The RMS values of the centroid acceleration, acceleration of the roll angle, and acceleration of the pitch angle of active suspension are 33.34%, 4.82%, and 4.10% higher than those of passive suspension, respectively.

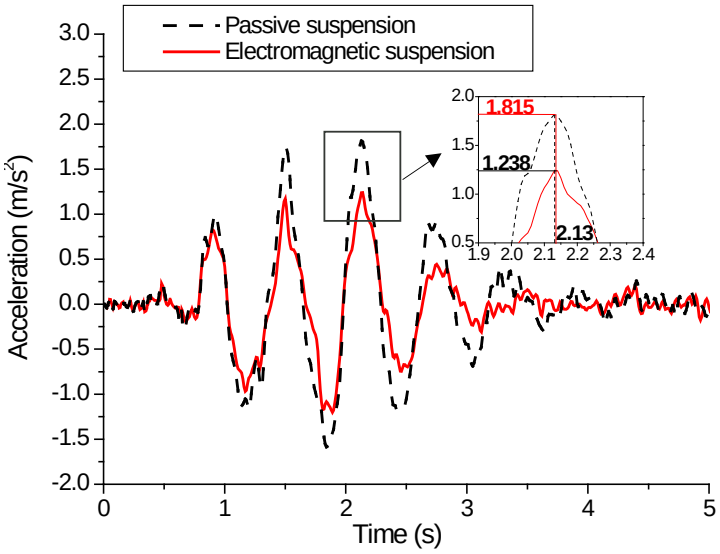

Figure 19. Centroid acceleration on a deceleration strip.

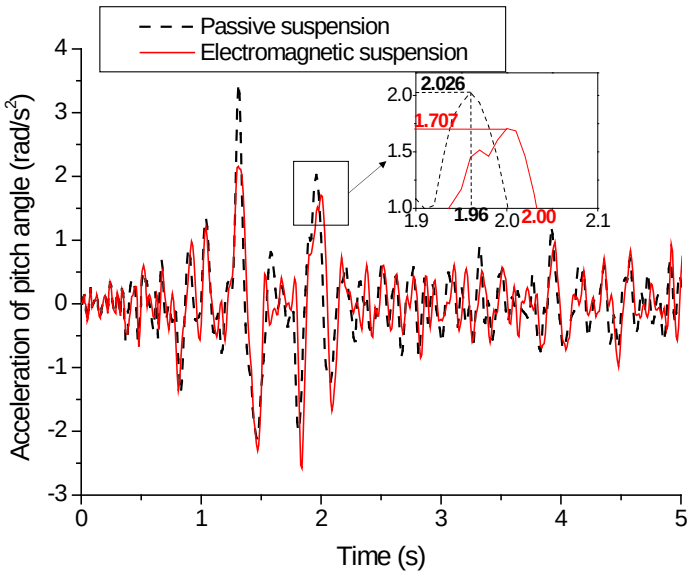

Figure 20. Acceleration of the roll angle on a deceleration strip.

The centroid acceleration result shows that the tracking performance of acceleration is good without any delay phenomena. At 2.13 s, the peak value of centroid acceleration using electromagnetic suspension is 0.557 m/s^2 smaller than when using passive suspension. In the simulation results of the acceleration of the roll angle, there is a slight delay, with a delay time of 0.04 s. The peak values of the accelerations of the roll angle and the pitch angle decreased by 0.319 rad/s^2 and 0.015 rad/s^2, respectively.

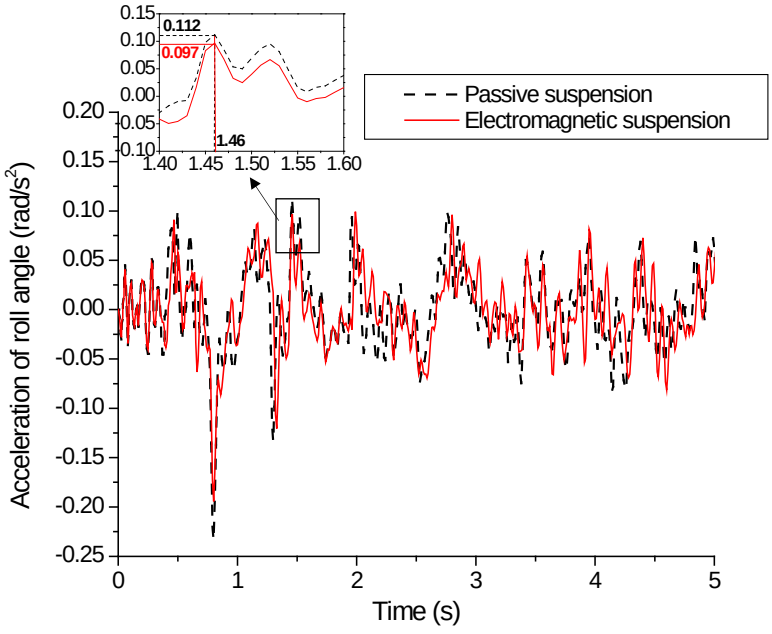

Figure 21. Acceleration of the pitch angle on a deceleration strip.

The dynamic deflections of the four wheels of the vehicle are shown in Figure 22. The RMS values of the dynamic deflection of wheels A, B, C, and D decreased by 21.26%, 21.40%, 25.01%, and 24.24%, respectively. When the rear wheels pass through the reducer, the shock absorbers generate a downward dynamic deflection. After fuzzy PID control, the dynamic deflections of the four dampers decrease by 0.0057 m, 0.0047 m, 0.0042 m, and 0.0026 m, respectively. The fluctuation of the rear wheel is delayed by 0.02 s relative to the fluctuation of the front wheel. The dynamic deflections of the four wheels of the passive suspension are −0.0148 m, −0.0155 m, −0.0127 m, and −0.0113 m, and it can be seen that the difference between the maximum and minimum is 0.0042 m. The dynamic deflections of wheels A, B, C, and D of the electromagnetic suspension are −0.0091 m, −0.0108 m, −0.0085 m, and −0.0087 m, and it can be seen that the difference between the maximum and minimum is 0.0023 m. These results indicate that electromagnetic suspension can be effectively controlled on a deceleration strip or when braking, which makes up for the poor stability of the MacPherson suspension.

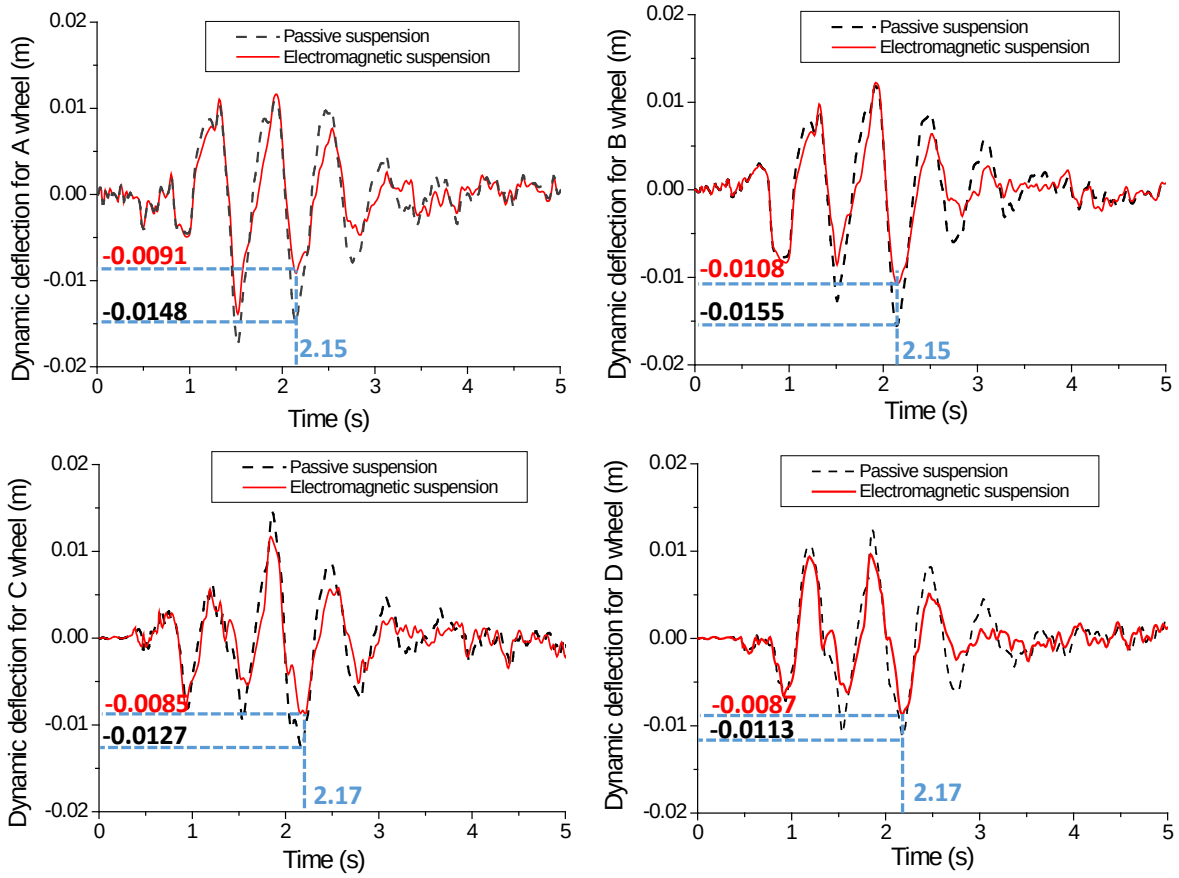

Figure 22. Dynamic deflections on a deceleration strip for four wheels.

The simulation results of the dynamic load for the four wheels are shown in Figure 23. The RMS values of the dynamic loads of wheels A, B, C, and D are 11.43%, 11.91%, 14.91%, and 15.03% lower than those of the passive suspension, respectively. When passing through the deceleration strip, the dynamic loads of the front wheel tires are larger than those of the rear wheel tires. The results show that when the vehicle passes through the deceleration strip, the dynamic load of the tires can be reduced and the excessive friction of the tires can be effectively prevented via the fuzzy PID control algorithm.

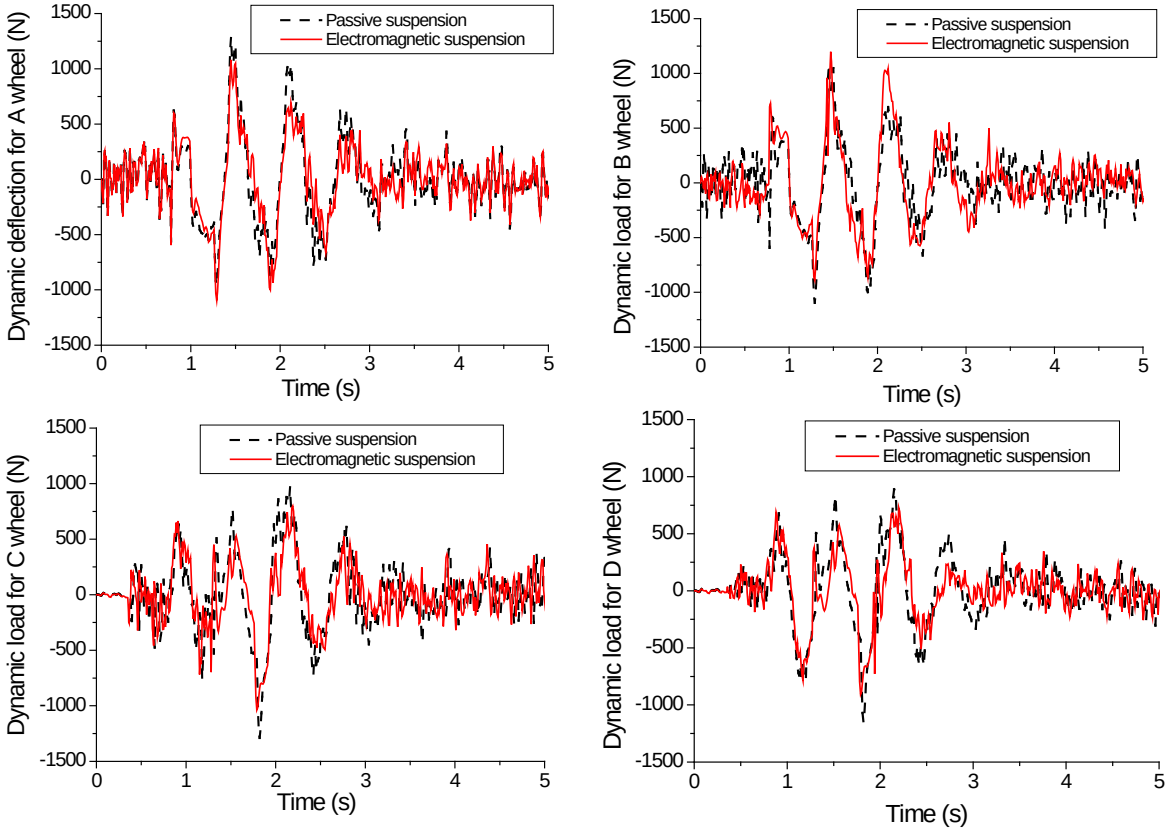

Figure 23. Dynamic loads on a deceleration strip for four wheels.

6. Conclusions

This paper proposes an electromagnetic suspension that can ensure the safety of a vehicle and improve the ride comfort and stability of the MacPherson suspension. This suspension does not change the safety of the MacPherson suspension with embedding an electromagnetic actuator. Once the electromagnetic actuator fails, the safety of the electromagnetic suspension can be guaranteed.

This paper mainly studies its magnetic characteristics and fuzzy PID control. First, an electromagnetic suspension is proposed, and its theoretical magnetic field model is established and analyzed. Second, on the basis of the electromagnetic suspension system, a FEM model is established, and the magnetic field, magnetic flux density, and magnetic force are simulated and analyzed. Finally, on the basis of the fuzzy PID control algorithm, a vehicle simulation analysis of the electromagnetic suspension is carried out. The results show that the magnetic field trends of the theoretical results and the finite element results are consistent via a comparison. The direction and the trend of the magnetic flux density in the FEM simulation show that the magnetic fluxes are parallel to each other in the air gap of the magnet assembly. Comparing the theoretical results, finite element results, and experimental results in [44], the electromagnetic suspension proposed in this paper owns a larger magnetic flux density in the air gap. At the same time, it can also prove the correctness of the trend of the theoretical results and the feasibility of the proposed electromagnetic actuator. Based on the fuzzy PID control algorithm, the vehicle dynamics of the electromagnetic suspension are simulated. The simulation results show that compared to a passive suspension system, RMS values of the acceleration, the acceleration of roll angle, and the acceleration of pitch angle for the vehicle body are reduced by 59.08%, 3.06%, and 3.54%, respectively, and the dynamic deflection of the four suspension systems and the dynamic load of the four wheels are reduced. Therefore, this control algorithm is suitable for an electromagnetic suspension system.

In the future, we will build an experimental prototype of this electromagnetic actuator for magnetic field and current experiments. At the same time, research is being conducted on the stability and smoothness control of electromagnetic suspension with extreme road surfaces.

Author Contributions: Conceptualization, W.W.; methodology, W.W.; software, W.W., S.Y. and B.L.; validation, B.L.; resources, W.W., S.Y. and B.L.; writing—original draft preparation, W.W. and B.L.; writing—review and editing, W.W. and S.Y.; supervision, W.W.; project administration, W.W.; funding acquisition, W.W. and S.Y. All authors have read and agreed to the published version of the manuscript.

Funding: This research was funded by Scientific Research Startup Project of Liaoning University of Technology (XB2021003).

Data Availability Statement: Not applicable.

Conflicts of Interest: The authors declare no conflict of interest.

References

1. Tseng, H.E.; Hrovat, D. State of the art survey: Active and semi-active suspension control. *Veh. Syst. Dyn.* **2015**, *53*, 1034–1062. [CrossRef]
2. Cao, D.; Song, X.; Ahmadian, M. Editors' perspectives: Road vehicle suspension design, dynamics, and control. *Veh. Syst. Dyn.* **2011**, *49*, 3–28. [CrossRef]
3. Kim, K.H.; Woo, D.K. Linear tubular permanent magnet motor for an electromagnetic active suspension system. *IET Electr. Power Appl.* **2021**, *15*, 1648–1665. [CrossRef]
4. Zhou, H.; Zhen, L.; Zhao, W.; Liu, G.; Xu, L. Design and analysis of low-cost tubular fault-tolerant interior permanent-magnet motor. *IEEE Trans. Magn.* **2016**, *52*, 8104804. [CrossRef]
5. Basaran, S.; Basaran, M. Vibration control of truck cabins with the adaptive vectorial backstepping design of electromagnetic active suspension system. *IEEE Access* **2020**, *8*, 173056–173067. [CrossRef]
6. Harikrishnan, P.M.; Varun, P.G. Vehicle vibration signal processing for road surface monitoring. *IEEE Sens. J.* **2017**, *17*, 5192–5197. [CrossRef]
7. Majdoub, K.E.; Giri, F.; Chaoui, F.Z. Adaptive backstepping control design for semi-active suspension of half-vehicle with magnetorheological damper. *IEEE/CAA J. Autom. Sin.* **2022**, *8*, 582–596. [CrossRef]
8. Envelope, K.; Envelope, K.H. Vibration control of semi-active suspension by the neural network that learned the optimal preview control of MLD model. *IFAC-Pap.* **2022**, *55*, 515–520.
9. Basargan, H.; Mihály, A.; Gáspár, P.; Sename, O. An LPV-based online reconfigurable adaptive semi-active suspension control with MR damper. *Energies* **2022**, *15*, 3648. [CrossRef]
10. Liu, W.; Wang, R.; Ding, R.; Meng, X.; Yang, L. On-line estimation of road profile in semi-active suspension based on unsprung mass acceleration. *Mech. Syst. Signal Process.* **2020**, *135*, 106370. [CrossRef]
11. Beno, J.H.; Weeks, D.A.; Bresie, D.A.; Guenin, A.M.; Wisecup, J.S.; Bylsma, W. Experimental comparison of losses for conventional passive and energy efficient active suspension systems. SAE Technical Paper Series. In Proceedings of the SAE International SAE 2002 World Congress & Exhibition, Detroit, MI, USA, 4 May 2002. SAE Technology Paper, 2002-01-0282.
12. Weeks, D.A.; Beno, J.H.; Guenin, A.M.; Bresie, D.A. Electro mechanical active suspension demonstration for off-road vehicles. In *Direct Injection SI Engine Technology, Proceedings of the SAE 2000 World Congress, Detroit, MI, USA, 6 March 2000*; SAE International: Warrendale, PA, USA, 2000; SAE Technology Paper, 2000-01-0102.
13. Bylsma, W.; Guenin, A.M.; Beno, J.H.; Weeks, D.A.; Bresie, D.A.; Raymond, M.E. Electromechanical suspension performance testing. SAE Technical Paper Series. In Proceedings of the 2001 SAE International SAE 2001 World Congress, Detroit, MI, USA, 5–8 March 2001. SAE Technology Paper, 2001-01-0492.
14. Hayes, R.J.; Beno, J.H.; Weeks, D.A.; Guenin, A.M.; Mock, J.R.; Worthington, M.S.; Triche, E.J.; Chojecki, D.; Lippert, D. Design and testing of an active suspension system for a 2-1/2 ton military truck. SAE Technology Paper. In Proceedings of the SAE International SAE 2005 World Congress & Exhibition, Detroit, MI, USA, 11 April 2005. SAE Technology Paper, 2005-01-1715.
15. Yu, F.; Cao, M.; Zheng, X.C. Research on the feasibility of vehicle active suspension with energy regeneration. *Vib. Shock.* **2005**, *24*, 27–30.
16. Yu, F.; Fang, T.; Pattipati, K.R. A novel congruent organizational design methodology using group technology and a nested genetic algorithm. *IEEE Trans. Syst. Man Cybern. Part A Syst. Hum.* **2005**, *36*, 5–18.
17. Zhang, Y.C.; Yu, F.; Gu, Y.H. Isolation and energy-regenerative performance experimental verification of automotive electrical suspension. *J. Shanghai Jiaotong Univ.* **2008**, *42*, 874–877.
18. Huang, K.; Yu, F.; Zhang, Y.C. Model predictive controller design for electromagnetic active suspension. *J. Shanghai Jiaotong Univ.* **2010**, *44*, 1619–1624.
19. Huang, S.J.; Chen, H.Y. Adaptive sliding controller with self-tuning fuzzy compensation for vehicle suspension control. *Mechatronics* **2006**, *16*, 607–622. [CrossRef]

20. Kawamoto, Y.; Suda, Y.; Inoue, H.; Kondo, T. Modeling of electromagnetic damper for automobile suspension. *J. Syst. Des. Dyn.* **2007**, *1*, 524–535. [CrossRef]
21. Hayashi, R.; Suda, Y.; Nakano, K. Anti-rolling suspension for an automobile by coupled electromagnetic devices. *J. Mech. Syst. Transp. Logist.* **2008**, *1*, 43–55. [CrossRef]
22. Kawamoto, Y.; Suda, Y.; Inoue, H.; Kondo, T. Electro-mechanical suspension system considering energy consumption and vehicle manoeuvre. *Veh. Syst. Dyn.* **2008**, *46*, 1053–1063. [CrossRef]
23. Asadi, E.; Ribeiro, R.; Khamesee, M.B.; Khajepour, A. Analysis, prototyping and experimental characterization of an adaptive hybrid-electromagnetic damper for automotive suspension systems. *IEEE Trans. Veh. Technol.* **2017**, *66*, 3703–3713. [CrossRef]
24. Liu, Y.; Xu, L.; Zuo, L. Design, modeling, lab, and field tests of a mechanical-motion-rectifier-based energy harvester using a ball-screw mechanism. *IEEE/ASME Trans. Mechatron.* **2017**, *22*, 1933–1943. [CrossRef]
25. Eckert, P.R.; Flores Filho, A.F.; Perondi, E.A.; Dorrell, D.G. Dual quasi-halbach linear tubular actuator with coreless moving-coil for semiactive and active suspension. *IEEE Trans. Ind. Electron.* **2018**, *65*, 9873–9883. [CrossRef]
26. Eckert, P.R.; Flores Filho, A.F.; Perondi, E.; Ferri, J.; Goltz, E. Design Methodology of a Dual-Halbach Array Linear Actuator with Thermal-Electromagnetic Coupling. *Sensors* **2016**, *16*, 360. [CrossRef] [PubMed]
27. Beltran-Carbajal, F.; Valderrabano-Gonzalez, A.; Favela-Contreras, A. An active vehicle suspension control approach with electromagnetic and hydraulic actuators. *Actuators* **2019**, *8*, 35. [CrossRef]
28. Ning, D.; Du, H.; Sun, S.; Zheng, M.; Li, W.; Zhang, N.; Jia, Z. An electromagnetic variable stiffness device for semiactive seat suspension vibration control. *IEEE Trans. Ind. Electron.* **2020**, *67*, 6773–6784. [CrossRef]
29. Wang, J.J.; Cai, Y.F.; Chen, L.; Shi, D.; Wang, S.; Zhu, Z. Research on compound coordinated control for a power-split hybrid electric vehicle based on compensation of non-ideal communication network. *IEEE Trans. Veh. Technol.* **2020**, *69*, 14818–14833. [CrossRef]
30. Wang, J.J.; Cai, Y.F.; Chen, L.; Shi, D.; Wang, R.; Zhu, Z. Review on multi-power sources dynamic coordinated control of hybrid electric vehicle during driving mode transition process. *Int. J. Energy Res.* **2020**, *44*, 6128–6148. [CrossRef]
31. Wei, W.; Li, Q.; Xu, F.; Zhang, X.; Jin, J.; Jin, J.; Sun, F. Research on an electromagnetic actuator for vibration suppression and energy regeneration. *Actuators* **2020**, *9*, 42. [CrossRef]
32. Wei, W.; Sun, F.; Jin, J.Q.; Zhao, Z.Y.; Miao, L.G.; Li, Q.; Zhang, X.Y. Proposal of energy-recycle type active suspension using magnetic force. *Int. J. Appl. Electromagn. Mech.* **2019**, *59*, 577–585. [CrossRef]
33. Ye, X.M.; Long, H.Y.; Pei, W.C.; Li, Y.G.; Zhang, S.; Chu, J. Fuzzy control of automotive magnetorheological semi-active suspension. *J. North China Univ. Sci. Technol.* **2018**, *40*, 79–87.
34. Bashir, A.O.; Rui, X.; Zhang, J. Ride comfort improvement of a semi-active vehicle suspension based on hybrid fuzzy and fuzzy-PID controller. *Stud. Inform. Control.* **2019**, *28*, 421–430. [CrossRef]
35. El-Taweel, H.; Elhafiz, M.; Metered, H. Vibration Control of Active Vehicle Suspension System Using Optimized Fuzzy-PID. SAE Technical Paper Series. In Proceedings of the WCX World Congress Experience, Detroit, MI, USA, 3 April 2018. SAE International by Univ of California Berkeley, 2018-01-1402.
36. Wang, X.; Yang, B.T.; Zhu, Y. Adaptive model-based feedforward to compensate Lorentz force variation of voice coil motor for the fine stage of lithographic equipment. *Optik* **2019**, *135*, 27–35. [CrossRef]
37. Lian, J.Q.; Xie, S.Y.; Wang, J. Analysis of cogging torque of PM motor with radial magnetic field and parallel magnetic field. *Appl. Mech. Mater.* **2011**, *105–107*, 2289–2294. [CrossRef]
38. Jing, L.B.; Zhang, Y.S.; Li, C.; Zhang, K. Magnetic field computa-tion and optimization design for a concentric magnetic gear with hal-bach permanent-magnet arrays. *Proc. CSEE* **2013**, *33*, 163–169.
39. Wang, X.; Yang, B.T.; Zhu, Y. Modeling and analysis of a novel rectan-gular voice coil motor for the 6-DOF fine stage of lithographic equip-ment. *Optik* **2016**, *127*, 2246–2250. [CrossRef]
40. Liu, Y.; Zhang, M.; Zhu, Y. Optimization of voice coil motor to enhance dynamic response based on an improved magnetic equivalent circuit model. *IEEE Trans. Magn.* **2011**, *47*, 2247–2251. [CrossRef]
41. Babic, S.I.; Akyel, C. Improvement in the Analytical Calculation of the Magnetic Field Produced by Permanent Magnet Rings. *Prog. Electromagn. Res. C* **2016**, *5*, 71–82.
42. Xia, Z.P.; Zhu, Z.Q.; Howe, D. Senior member. analytical magnetic Field analysis of halbach Magnetized permanent-magnet machines. *IEEE Trans. Magn.* **2004**, *40*, 1864–1872. [CrossRef]
43. Chen, Y.; Zhang, K.L. Analytic calculation of the magnetic field created by Halbach permanent magnets array. *J. Magn. Mater. Devices* **2014**, *45*, 1–4.
44. Wei, W.; Li, Q.; Sun, F.; Zhang, X.Y. Vibration control and energy regeneration of active suspension based on electromagnetic actuator—Development of electromagnetic actuator. In Proceedings of the International Conference on Precision Engineering (ICPE), Hakodate, Japan, 5–7 September 2018. C03-1.